metals

MDPI

Article

Oxidation and Microstructural Evolution of GTD-111 at 850 °C and 1000 °C

Odnyam Renchindorj [1,†], Nomin-Erdene Battulga [1,†], Yinsheng He [2], Youngdae Kim [3], Yeonkwan Kang [3], Jinesung Jung [3], Keesam Shin [1,4,*] and Je-Hyun Lee [1,4,*]

[1] Department of Materials Convergence and System Engineering, Changwon National University, Changwon 51140, Republic of Korea; odnyamr335@gmail.com (O.R.); battnominerdene@gmail.com (N.-E.B.)
[2] National Center for Materials Service Safety, University of Science and Technology Beijing, Beijing 100083, China; heyinsheng@ustb.edu.cn
[3] Power Generation Technology Laboratory, Korea Electric Power Research Institute, Daejeon 34056, Republic of Korea; youngdae1.kim@kepco.co.kr (Y.K.); yeonkwan.kang@kepco.co.kr (Y.K.); jinesung.jung@kepco.co.kr (J.J.)
[4] School of Materials Science and Engineering, Changwon National University, Changwon 51140, Republic of Korea
* Correspondence: keesam@changwon.ac.kr (K.S.); ljh@changwon.ac.kr (J.-H.L.)
† These authors contributed equally to this work.

Abstract

The oxidation behavior and microstructures of the GTD-111 Ni-based superalloy were investigated following heat treatment at 850 °C and 1000 °C for up to 5000 h, using Optical Microscopy (OM), X-Ray Diffraction (XRD), Scanning Electron Microscopy (SEM), Energy Dispersive Spectroscopy (EDS), and Transmission Electron Microscopy (TEM). SEM/EDS analysis showed that the microstructure of the samples mainly consisted of γ' precipitates in the matrix, eutectic phases, and several types of carbides. Cross-sectional analysis revealed that the oxidation region was composed of three layers: a top layer (NiO, TiO_2, Cr_2O_3), a sublayer (Ta_2O_5, TiO_2), and an inner layer (Al_2O_3), followed by a needle-like Ti-containing phase. The oxidation kinetics followed the parabolic law as a function of time at each temperature. After the heat treatments, the dendritic regions of all specimens consisted of cuboidal primary γ' precipitates and spherical secondary γ' precipitates. Chinese-script-like and blocky-shaped MC carbides, as well as three types of $M_{23}C_6$ carbides, were found in the interdendritic region. The fracture mode of the tensile specimens transformed from cleavage (brittle) fracture to ductile fracture as the temperature increased. Cracks were observed inside the MC carbides on the fracture surface, which may serve as significant crack initiation sites.

Keywords: nickel-based superalloy; heat treatment; oxidation layer; kinetics; gamma prime; tensile; stress-rupture

Check for updates

Academic Editor: Rebecca L. Higginson

Received: 12 November 2025
Revised: 17 December 2025
Accepted: 19 December 2025
Published: 23 December 2025

Copyright: © 2025 by the authors. Licensee MDPI, Basel, Switzerland. This article is an open access article distributed under the terms and conditions of the Creative Commons Attribution (CC BY) license.

1. Introduction

Nickel-based superalloys are extensively used for gas turbine and jet engine blades due to their high oxidation resistance, corrosion resistance, and excellent mechanical properties at high temperatures [1].

Alloying elements such as Mo, W, Ta, Re, and Nb are commonly added to improve mechanical properties via solid solution hardening, while Al and Ti facilitate precipitation strengthening of the γ' phase in the Ni matrix. Carbon is added to improve grain boundary

properties, whereas Al and Cr are included to enhance oxidation resistance. The characterization of oxide films typically focuses on chemical composition, microstructure, and thickness, while oxidation kinetics are evaluated through mass change [2].

Understanding the oxide growth kinetics of high-temperature Ni-based superalloys is essential for component maintenance and life extension. GTD-111, a precipitation-strengthened alloy developed in the 1970s for high-power land-based gas turbines, contains ~14 wt.% Cr along with significant amounts of Co, Mo, W, Ta, Al, and Ti. This composition yields a high volume fraction of γ' precipitates (~60%) and complex interdendritic carbides, resulting in tensile, creep, and corrosion properties superior to those of earlier alloys like IN738LC and René 80 [3–5]. Widely used for first-stage blades in both conventionally cast and directionally solidified forms [4,6,7], GTD-111 combines excellent performance with cost-effective castability and reparability. Consequently, characterizing its long-term oxidation and microstructural evolution is critical for reliable life assessment and repair optimization [5,8,9].

GTD-111 possesses yield and tensile strengths superior to IN-738LC and comparable to René 80, attributed to a higher γ' precipitate volume fraction (~60% vs. ~45% in IN-738LC). This results in a ~20 °C advantage in operating temperature over IN-738LC for equivalent rupture life [3]. Additionally, GTD-111 exhibits hot corrosion resistance (800–950 °C) comparable to IN-738LC, despite lower Cr content (14% vs. 16%), making it far superior to the corrosion-prone René 80 in the low-grade fuel environments [10].

While thermodynamics determines oxide stability via the Gibbs free energy of formation, kinetics governs the rate of oxide layer growth—a critical factor in the high-temperature degradation of Ni-based superalloys. The formation of protective scales, such as Al_2O_3 and Cr_2O_3, is essential for the oxidation resistance of these materials [11]. Accordingly, most studies assess oxidation kinetics through mass change [12,13] or scale thickness measurements [14,15].

Only a few studies have focused on the mechanical properties, fracture behavior, and structural stability of GTD-111 [16,17]. Similarly, a limited number of oxidation studies are available for this alloy, such as those examining oxidation mechanisms at 900 °C [8,18] and 1100 °C [19], or focusing on TBC-coated systems [20]. There are currently few reports on the long-term oxidation behavior of bare GTD-111 at high temperatures, as most existing studies focus on short-term behavior (<400 h). Thus, further understanding is required regarding the stability of phases such as γ' and carbides in GTD-111 during high-temperature exposure. This work aims to investigate the oxidation behavior and the effects of heat treatment on the microstructure and tensile properties of GTD-111 Ni-based superalloy at 850 °C and 1000 °C.

2. Materials and Methods

2.1. Materials

The nominal chemical composition of GTD-111 specimens is listed below (Table 1).

Table 1. Nominal chemical composition of GTD-111. Data from Refs. [8,19–22].

Alloy	Cr	Co	Mo	W	Al	Ti	Ta	C	Zr	Ni
GDT-111	13.6–14.1	9.5–10.8	1.38–1.60	3.0–4.4	3.0–4.0	2.7–5.1	2.54–4.70	0.07–0.10	0.02–0.03	Bal.

The specimens were prepared by heat treatment at 850 °C and 1000 °C for 50 h, 100 h, 250 h, 500 h, 1000 h, 3000 h, and 5000 h with subsequent air cooling.

2.2. Specimens for Tensile Test and Microstructural Analysis

1. Sample Preparation
   (1) Specimens for SEM analysis were sectioned, mounted, and mechanically polished using SiC sandpaper (grades #220 to #2000), followed by polishing with 3 μm and 1 μm alumina suspensions. The specific specimen groups included:
   (2) Oxidation Specimens: Circular disks (∅12.4 mm) heat-treated at 850 °C and 1000 °C for up to 5000 h. These were sectioned diametrically to obtain a cross-section of ~6.2 × 3.2 mm^2.
   (3) Tensile Specimens: Samples obtained from tensile tests performed on both airfoil and root sections at 25 °C, 800 °C, and 900 °C.
   (4) Stress-Rupture Specimens: Samples obtained from stress-rupture tests conducted at 816 °C, 871 °C, 926 °C, and 982 °C.
2. Microstructural Characterization

Microstructural and compositional characterizations were performed using Optical Microscopy (HI MAX Tech, Seoul, Republic of Korea), SEM (JEOL JSM-7900F, Tokyo, Japan) operating at 20 kV, EDS (Oxford X-Max 80, High Wycombe, UK), TEM (JEOL 2100F, Tokyo, Japan) and XRD (Rigaku SmartLab SE, Tokyo, Japan).

For microstructural observation, SEM samples were chemically etched using K2 solution (94 mL perchloric acid, 878 mL ethanol, 120 mL 2-butoxyethanol, and 108 mL distilled water). TEM specimens were prepared using FIB of Ga^+. The constituent phases of the oxide layer were identified by XRD using Cu Kα radiation (λ = 1.54056 Å) over a 2θ range of 10–110° with a step size of 0.02°. Particle characteristics were measured from SEM micrographs using ImageJ 1.8.0 software.

3. Results and Discussion

3.1. XRD Analysis of the Oxide Layer

Figure 1 shows the XRD patterns of the surface regions of the GTD-111 circular plates. The results indicate that the carbides and oxides formed are consistent across the specimens. In addition to the γ matrix (FCC, a = 3.52 Å) and the primary strengthening γ′ phase (FCC, a = 3.55 Å), oxides such as NiO (JCPDS 47-1049), Ta_2O_5 (JCPDS 25-0922), $NiCr_2O_4$ (JCPDS 75-1728), TiO_2 (JCPDS 21-1276), Cr_2O_3 (JCPDS 38-1479), Al_2O_3 (JCPDS 46-1212), as well as carbides like TiC (JCPDS 32-1383) and $Cr_{23}C_6$ (JCPDS 35-0783), were identified after heat treatment at 850 °C.

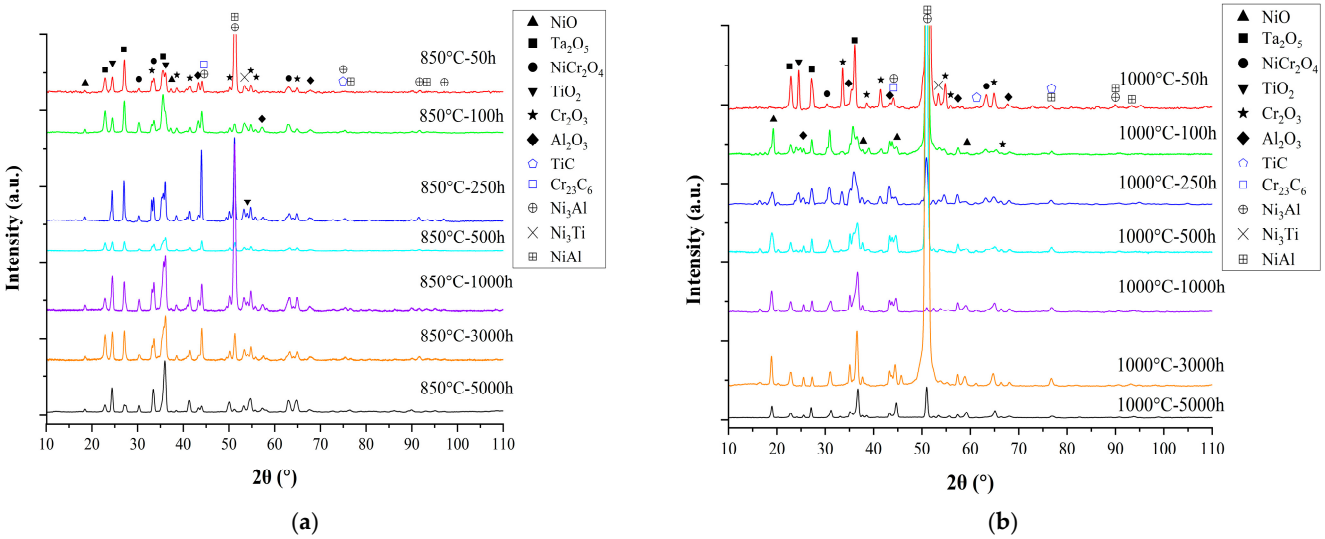


Figure 1. XRD results of the heat-treated specimens (**a**) at 850 °C and (**b**) 1000 °C.

The highest intensity peak observed at 2θ = 51.32° corresponds to the {002} planes of the γ and γ′ phases, which are the main constituents of the superalloy microstructure. Due to the similarity in lattice parameters between the γ and γ′ phases, their diffraction peaks overlap and are not resolved separately in the spectra. Furthermore, intensity variations in the γ, γ′ peaks are attributed to differences in growth orientation (texture) within the bulk specimens. The XRD results confirm that the types of secondary phases formed remain consistent across all test temperatures.

Notably, Al_2O_3 and TiO_2 peaks emerged after 100 h at 850 °C (2θ = 57.23°) and after 250 h at 850 °C (2θ = 53.98°), respectively. In the specimen heat-treated at 1000 °C for 50 h, the observed phases included the γ matrix, γ′ phase, oxides (Ta_2O_5, $NiCr_2O_4$, TiO_2, Cr_2O_3, Al_2O_3), and carbides (TiC, $Cr_{23}C_6$). With increasing exposure time at 1000 °C, additional oxide peaks became prominent: NiO peaks appeared after 100 h (at 18.86°, 37.86°, 44.42°, and 58.87°), while distinct Al_2O_3 and Cr_2O_3 peaks were observed after 100 h at 25.78° and 66.50°, respectively. The diffraction intensity of $NiCr_2O_4$ was higher than that of Al_2O_3, which can be attributed to the following formation reaction (1):

$$Cr_2O_3 + NiO \rightarrow NiCr_2O_4 \quad (1)$$

As oxidation progressed, the intensities of the matrix peaks decreased concomitantly with the thickening of the oxide layers.

3.2. Microstructure and Kinetics of the Oxide Layer in the Surface Region

3.2.1. Microstructure of the Oxide Layer in the Surface Region

The typical cross-section morphologies of the 850 °C and 1000 °C specimens are shown in Figure 2. At 850 °C, the oxide scale was composed of three distinct regions: an outermost layer of NiO, TiO_2, and Cr_2O_3; a sublayer containing Ta_2O_5 and TiO_2; and a discontinuous inner layer of Al_2O_3. The oxide scale formed at 1000 °C exhibited an identical layered structure and phase composition, with the notable exception that the inner Al_2O_3 layer was continuous rather than discontinuous. This observation is in good agreement with previous reports by Yu et al. and Brenneman et al. [23,24].

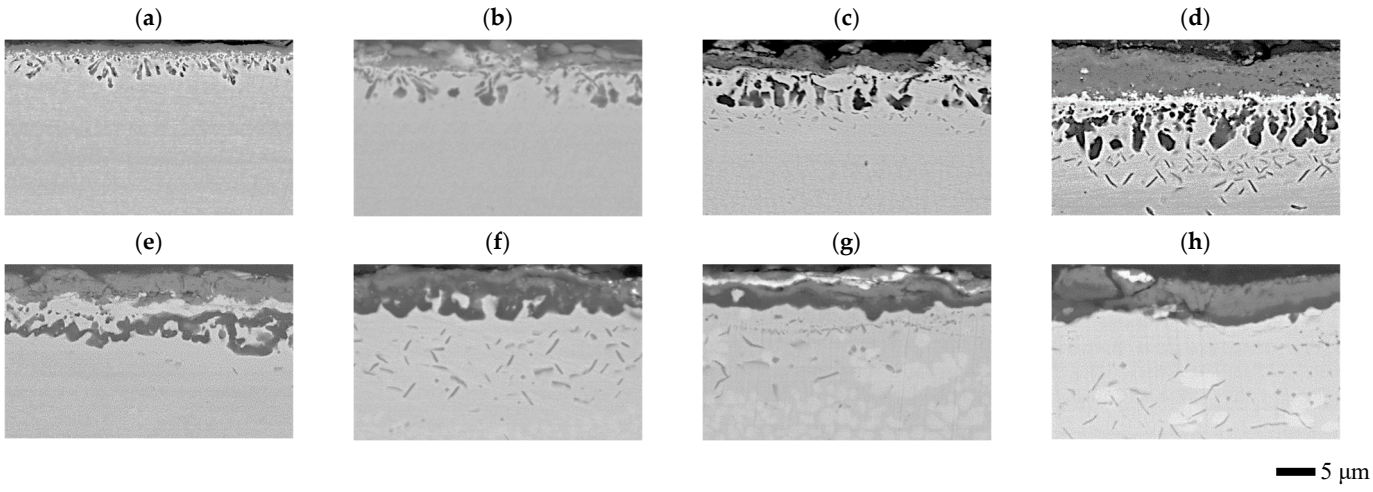


Figure 2. Backscattered SEM micrographs of the oxide layers of the 850 °C and 1000 °C specimens at different durations: (**a**) 850 °C-50 h; (**b**) 850 °C-250 h; (**c**) 850 °C-1000 h; (**d**) 850 °C-5000 h; (**e**) 1000 °C-50 h; (**f**) 1000 °C-250 h; (**g**) 1000 °C-1000 h; (**h**) 1000 °C-5000 h.

The SEM/EDS elemental mapping of the 850 °C-5000 h and 1000 °C-5000 h specimens are shown in Figure 3. The gray, needle-like precipitates observed below the Al_2O_3 layer in Figure 2c–h were identified as TiN, as confirmed by EDS elemental mapping

(Figure 3). TiN precipitates were detected in specimens heat-treated from 850 °C-1000 h up to 1000 °C-5000 h. This formation is attributed to the partial pressure of nitrogen being sufficiently high to promote nitrogen solubility from the air into the metal substrate beneath the oxide scale, a phenomenon also reported by other researchers [25,26].

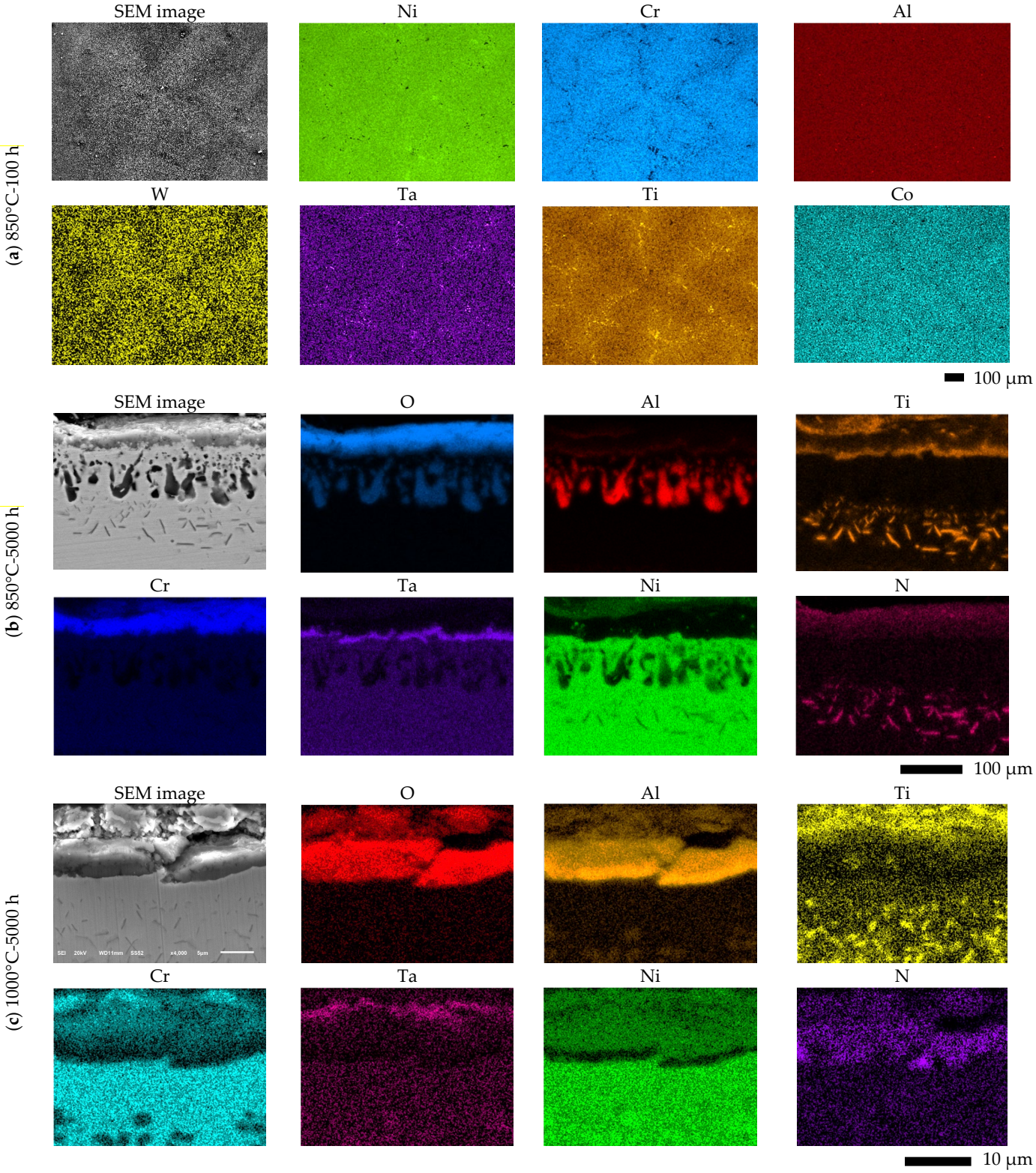


Figure 3. SEM/EDS elemental mapping of the oxide layer of the heat-treated specimen at (**a**) 850 °C-100 h, (**b**) 850 °C-5000 h and (**c**) 1000 °C-5000 h.

The presence of these specific oxides in the surface layers suggests that the constituent elements (Ni, Cr, Ti, Ta, and Al) diffuse outwardly from the substrate to the surface during oxidation, with diffusion rates varying as a function of temperature and time. The SEM/EDS elemental mapping of the dendritic microstructure in the specimen heat-treated at 850 °C for 100 h reveals that W and Cr are concentrated in the dendrite cores, whereas higher concentrations of Ti and Ta are observed in the interdendritic regions (Figure 3a). This segregation behavior is consistent with findings by Szczotok et al. and Strutt et al., who also reported that Re and W segregate to the dendrite cores, while Al and Ta segregate to the interdendritic regions [27–29].

The detailed morphology of the inner oxide scale following long-term exposure is further illuminated by the TEM observations presented in Figures 4 and 5. Figure 4 displays a cross-sectional TEM image of the specimen oxidized at 850 °C for 5000 h, revealing the formation of a thin, locally discontinuous Al_2O_3 layer at the metal-oxide interface, accompanied by needle-like TiN precipitates situated immediately beneath this layer. The close contact between the Al_2O_3 islands, the adjacent TiN particles, and the underlying matrix confirms that both phases nucleate at or near the interface during prolonged exposure.

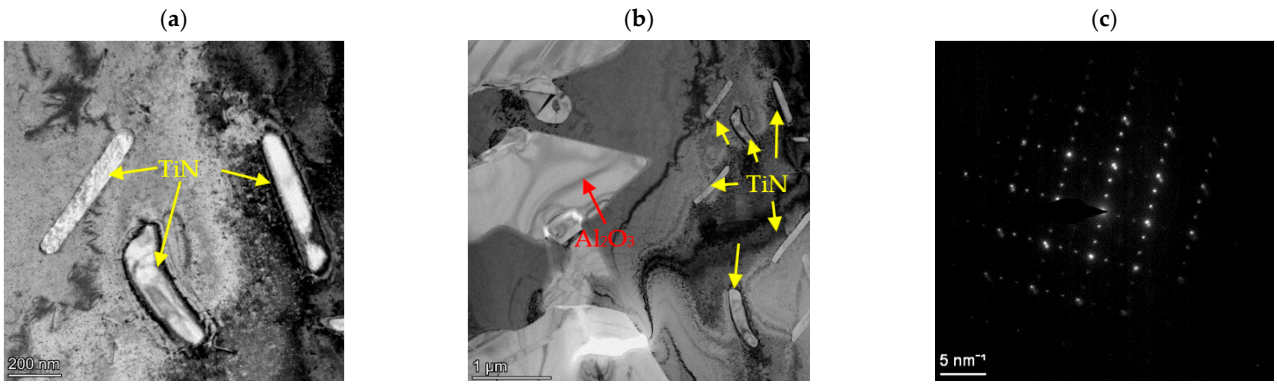


Figure 4. TEM micrograph of the heat-treated specimen at 850 °C-5000 h: (**a**) needle-like TiN; (**b**) needle-like TiN and Al_2O_3 island; (**c**) SAED pattern of Al_2O_3 island.

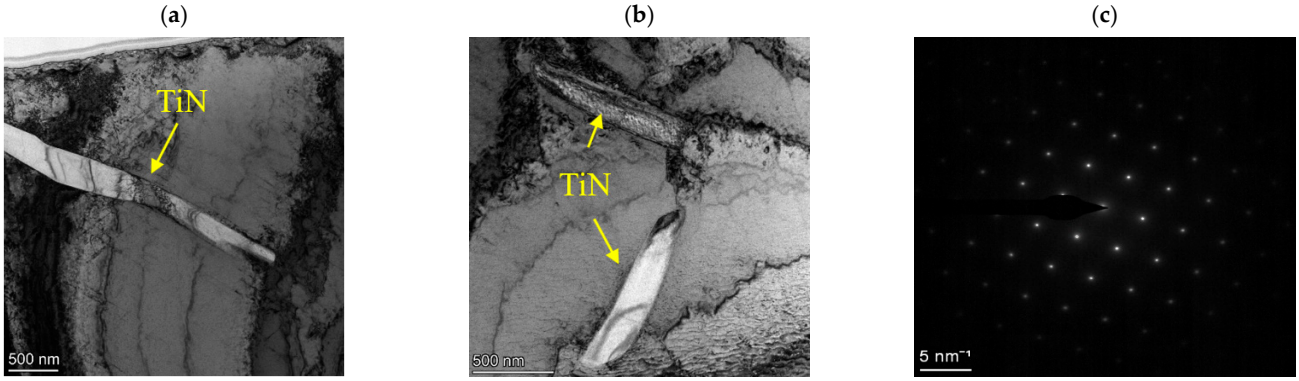


Figure 5. TEM micrograph of the heat-treated specimen at 1000 °C-5000 h: (**a**,**b**) needle-like TiN; (**c**) SAED pattern of needle-like TiN.

In contrast, Figure 5 demonstrates that after exposure to 1000 °C for 5000 h, the Al_2O_3 layer coalesces into a continuous inner oxide scale, with TiN precipitates again located beneath the alumina. This continuous Al_2O_3 layer acts as a more effective diffusion barrier; however, its formation is also consistent with the accelerated oxidation kinetics and more extensive internal oxidation observed at 1000 °C compared to 850 °C.

3.2.2. Kinetics of the Oxide Layer in the Surface Region

The oxidation kinetics at 850 °C and 1000 °C are presented in Figure 6. The plot confirms that the total oxide layer thickness increased with increasing temperature and time.

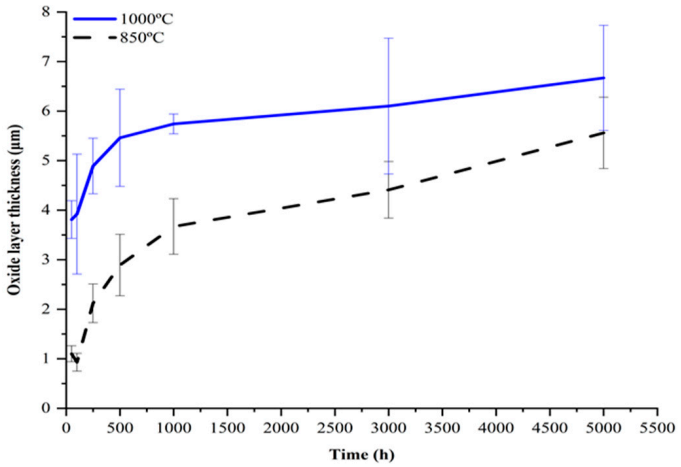


Figure 6. Thicknesses of the total oxide layers of the heat-treated specimens at 850 °C and 1000 °C.

The relationship between oxide thickness and oxidation time for both temperatures was found to follow the parabolic rate law. The parabolic rate constant (K) was calculated according to Equation (2) [13,14,20]:

$$d^2 = K \times t \tag{2}$$

where d is the total oxide layer thickness, K is the parabolic rate constant, and t is the oxidation time in hours. As shown in Figure 6, the oxide layer thickness for the 1000 °C specimen was significantly greater than that of the 850 °C specimen.

The temperature dependence of the parabolic rate constant can be expressed by the following equations:

$$K = A\ (p_{O_2})^n exp\ (-\frac{\Delta E}{RT}) \tag{3}$$

$$K = A \times \exp\ (-\frac{\Delta E}{RT}) \tag{4}$$

$$\ln K = -\frac{\Delta E}{R} \times \frac{1}{T} + \ln A \tag{5}$$

where A is the Arrhenius constant, ΔE is the activation energy, p_{O_2} is the oxygen partial pressure, n is the reaction order with respect to p_{O_2}, R = 8.314 J/(mol·K) is the gas constant and T is the absolute temperature. In the present work all oxidation tests were carried out in static laboratory air at 1 atm ($p_{O_2} \approx 0.21$ atm), the factor $(p_{O_2})^n$ is constant and is included in the Arrhenius constant. Therefore, the exponent n could not be determined experimentally. Nevertheless, changes in p_{O_2} are expected to modify both the defect structure of the oxide scale and the relative amounts of Ni, Cr, and Al-rich oxides, and thus influence the oxidation kinetics. The values of K for the oxidation tests are shown in Table 2 and Figure 7.

Table 2. The rate constants.

T, °C	1/T, 1/K	K, μm²/h	ln K, μm²/h
850	8.9×10^{-4}	0.0173	−4.0572
1000	7.86×10^{-4}	0.2903	−1.2368

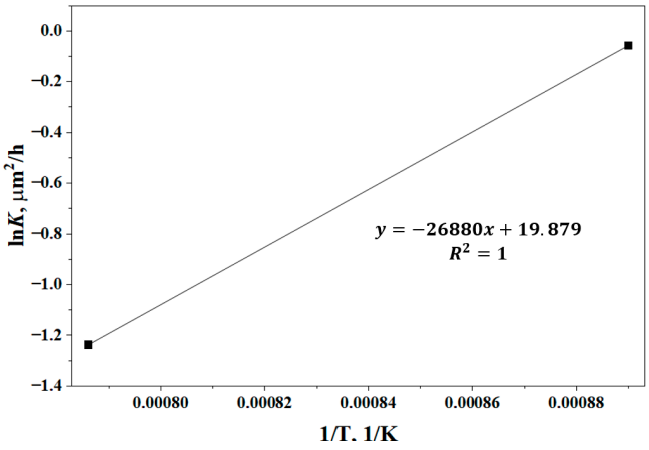


Figure 7. Linear fit of ln K and 1/T of GTD-111.

The oxide layer thicknesses formed at 850 °C and 1000 °C after 50 h were measured as 0.93 μm and 3.81 μm, respectively (Figure 6). Substituting these values into Equation (2), the K were calculated to be 0.0173 $\mu m^2/h$ and 0.2903 $\mu m^2/h$, respectively. Subsequently, by applying the values of K into Equation (2), A and ΔE were determined as 19.88 $\mu m^2/h$ and 223.5 kJ/mol, respectively. The calculated activation energy of 223.5 kJ/mol is close to the diffusion activation energy for Cr^{3+} diffusion in the oxide layer (255 kJ/mol) [30]. This suggests that the oxidation process is limited by the outward diffusion of Cr^{3+} ions through the oxide scale [31,32]. These results are comparable to those reported for chromia-forming ferritic stainless steels, such as Sanergy HT and Crofer 22H, which exhibit K values of approximately $\sim 2.7 \times 10^{-3}$ $\mu m^2/h$ at 850 °C in air containing 3% H_2O. This comparison indicates that the oxide layer on GTD-111 follows oxidation kinetics similar to those of other Cr_2O_3-forming alloys, further supporting the conclusion that scale growth is controlled by Cr^{3+} diffusion through a protective chromia-based scale [33].

In the context of metal oxidation, the Ellingham-Richardson diagram is widely utilized to evaluate the standard Gibbs free energy of formation (ΔG^0) and determine the thermodynamic stability of oxide species. The ΔG^0 values for NiO, Cr_2O_3, Al_2O_3, TiO_2, and Ta_2O_5 are expressed as a function of temperature (T) as follows [27]:

$$2Ni + O_2 = 2NiO, \quad \Delta G_T^0 = -497.16 + 0.1887T \left(\frac{kJ}{mol}\right) \tag{6}$$

$$\frac{4}{3}Cr + O_2 = \frac{2}{3}Cr_2O_3, \quad \Delta G_T^0 = -753.12 + 0.1826T \left(\frac{kJ}{mol}\right) \tag{7}$$

$$\frac{4}{5}Ta + O_2 = \frac{2}{5}Ta_2O_5, \quad \Delta G_T^0 = -773.35 + 0.1851T \left(\frac{kJ}{mol}\right) \tag{8}$$

$$Ti + O_2 = TiO_2, \quad \Delta G_T^0 = -944.75 + 0.1854T \left(\frac{kJ}{mol}\right) \tag{9}$$

$$\frac{4}{3}Al + O_2 = \frac{2}{3}Al_2O_3, \quad \Delta G_T^0 = -1116.29 + 0.2088T \left(\frac{kJ}{mol}\right) \tag{10}$$

Based on Equations (6)–(10), the standard Gibbs free energies for the five oxides were calculated over the temperature range of 100 K to 1400 K, as presented in Table 3 and Figure 8. It is evident that all calculated free energy values are negative, indicating that the oxidation reactions for these alloying elements are thermodynamically favorable (spontaneous) across the examined temperatures.

Table 3. Gibbs free energy of the oxidation reaction.

Temperature, °C	Gibbs Free Energy, ΔG^0 kJ/mol				
	NiO	Cr_2O_3	Ta_2O_5	TiO_2	Al_2O_3
850	−285.22	−548.03	−565.45	−736.52	−881.77
1000	−256.92	−520.64	−537.70	−708.71	−850.45

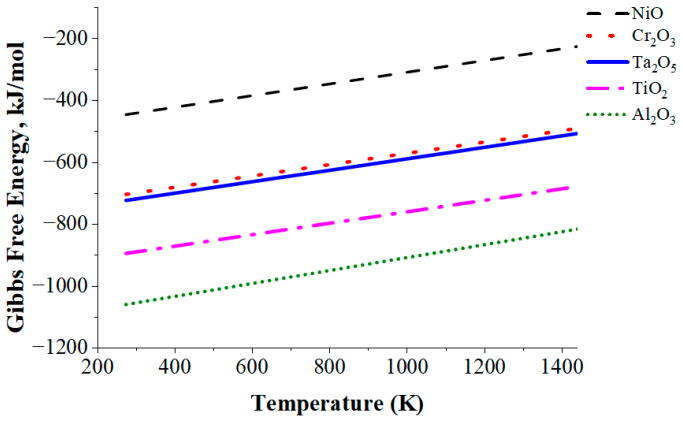


Figure 8. The value of Gibbs free energy for the relevant oxides.

The results reveal that the order of increasing thermodynamic stability for the oxides is NiO, Cr_2O_3, Ta_2O_5, TiO_2, and Al_2O_3. This hierarchy is consistent with the microstructural observations from SEM analysis. Equations (6)–(10), Table 3, and Figure 8 indicate that the relative ranking of ΔG^0 values does not change across the entire temperature range; meaning there are no crossovers in stability lines (and thus no changes in the relative driving forces) between 100 K and 1400 K. In this regard, the XRD phase identification results are in good agreement with the calculated ΔG^0 values.

The microstructure of the oxide layer and the proposed oxidation mechanism, based on the findings of this research, are schematically summarized in Figure 9.

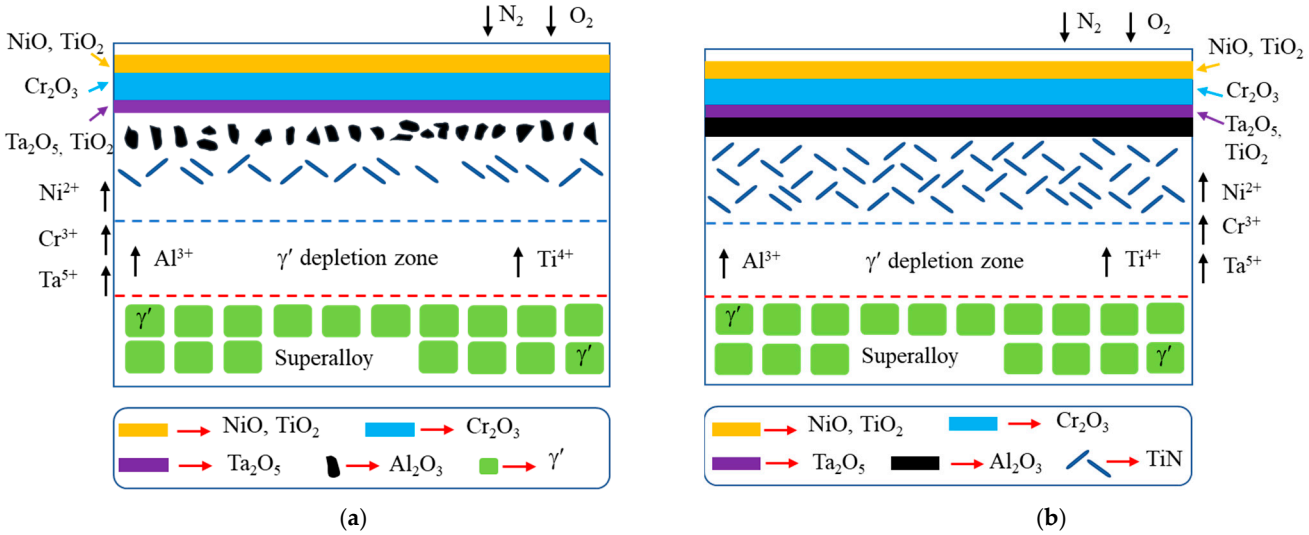


Figure 9. Proposed mechanisms for the formation of the oxide layers of the heat-treated specimens (**a**) at 850 °C and (**b**) at 1000 °C. The dash lines are defining the gamma prime depletion zone between oxidation layer and superalloy itself.

At high temperatures, metal (Ni, Ti, Cr, Ta, Al) cations diffuse outward from the matrix. Simultaneously, oxygen and nitrogen anions from the air diffuse inward into the specimens,

initiating the formation of oxide layers in the surface region. Over time, as the thickness of the oxide layer increases, it acts as a diffusion barrier, causing the oxidation rate to decrease.

3.3. Microstructure of the γ′ Precipitates

Figure 10a presents a typical SEM micrograph of the K2-etched circular plates, displaying a dendritic microstructure containing carbides. The higher magnification image, Figure 10b, reveals the detailed distribution of the γ′ phase, γ/γ′ eutectic phase, and carbides within the matrix. The carbides were predominantly located in the interdendritic regions, which appear darker than the dendrite cores. This difference in contrast is attributed to compositional segregation between the dendritic and interdendritic areas.

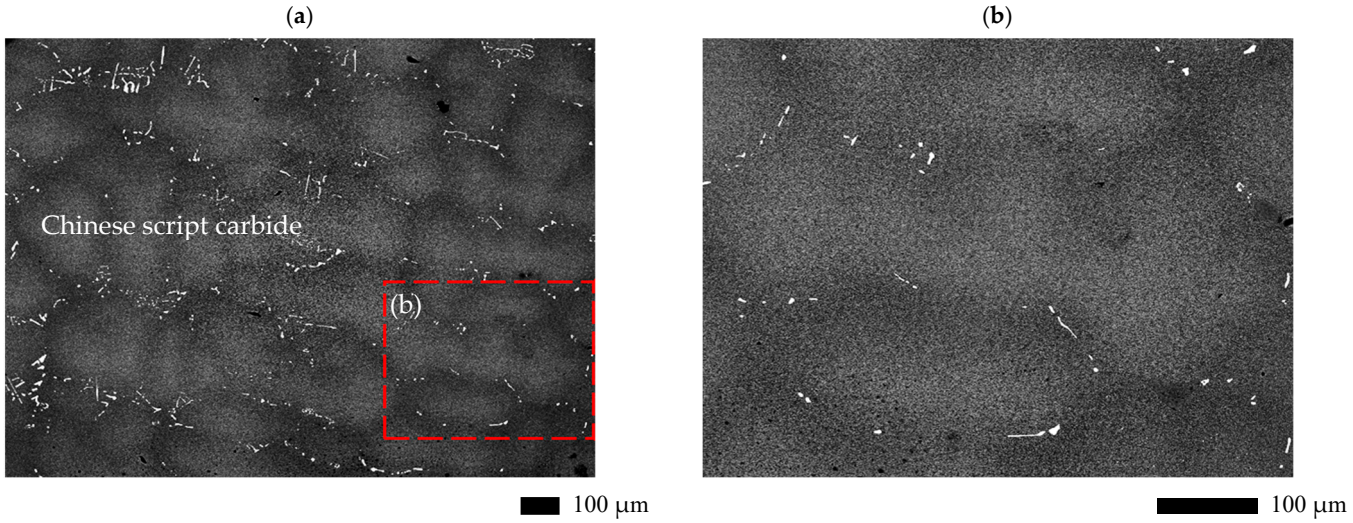


Figure 10. SEM micrographs of the dendrite microstructures of the heat-treated specimen at 850 °C-100 h: (**a**) low-magnified backscattered SEM micrograph and (**b**) enlarged backscattered SEM micrograph.

The evolution of the γ′ precipitate morphology for the 850 °C and 1000 °C specimens is presented in Figure 11. The results demonstrate that the size and morphology of the γ′ phase changed significantly upon heat treatment. Specifically, the γ′ precipitates coarsened (grew larger) as the exposure temperature and time increased. Figure 11 reveals that the primary γ′ precipitates are cuboidal, whereas the secondary γ′ precipitates are spherical. At 850 °C, the γ′ morphology evolved from cuboidal to a blocky shape with increasing heat-treatment time.

In contrast, the shapes of the γ′ precipitates at 1000 °C remained largely similar, though their sizes increased. Notably, in the 1000 °C specimens, there were regions of aligned γ′ precipitates separated by widened matrix channels, indicating the very early stages of rafting. This observation aligns with earlier reports of rafting in Ni-based superalloys above 900 °C [34].

As shown in Figure 12, the size of the γ′ precipitates increased with both temperature and time. Consequently, the γ′ precipitates in the 1000 °C specimens were significantly larger than those in the 850 °C specimens. Spatially, the γ′ precipitates in the interdendritic regions were observed to be coarser (larger) than those in the dendrite cores. The solidification sequence is believed to proceed as follows: γ(dendrite)⟶ γ(interdendrite)⟶ γ + γ′(eutectic)⟶ γ′(interdendrite)⟶ γ′(dendrite). Consistent with this sequence, the interdendritic regions are characterized by a microstructure containing larger γ′ precipitates compared to the dendritic cores [35].

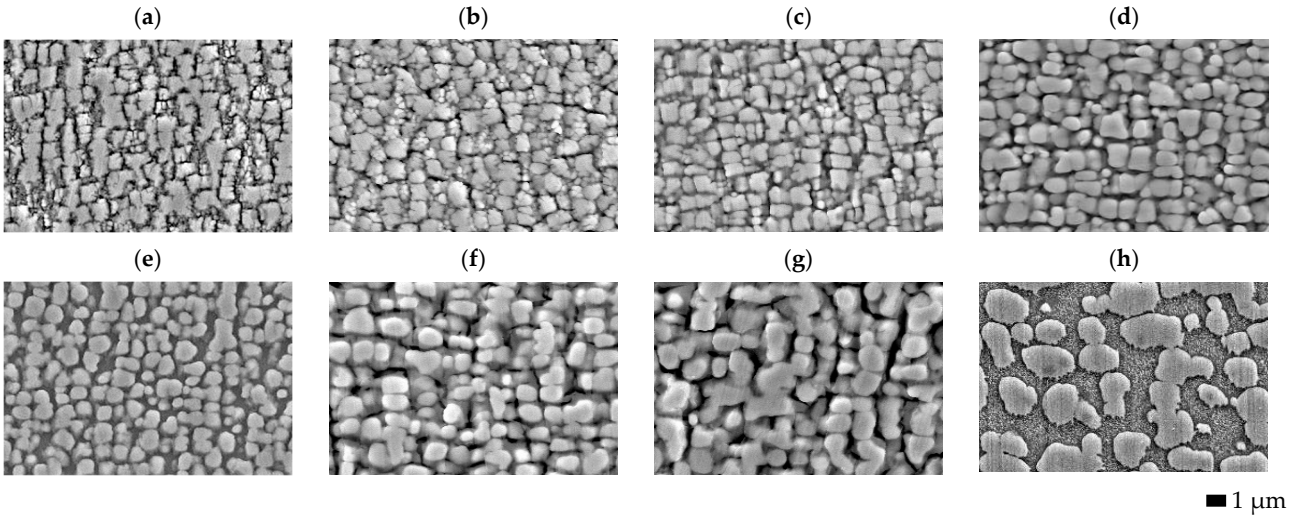
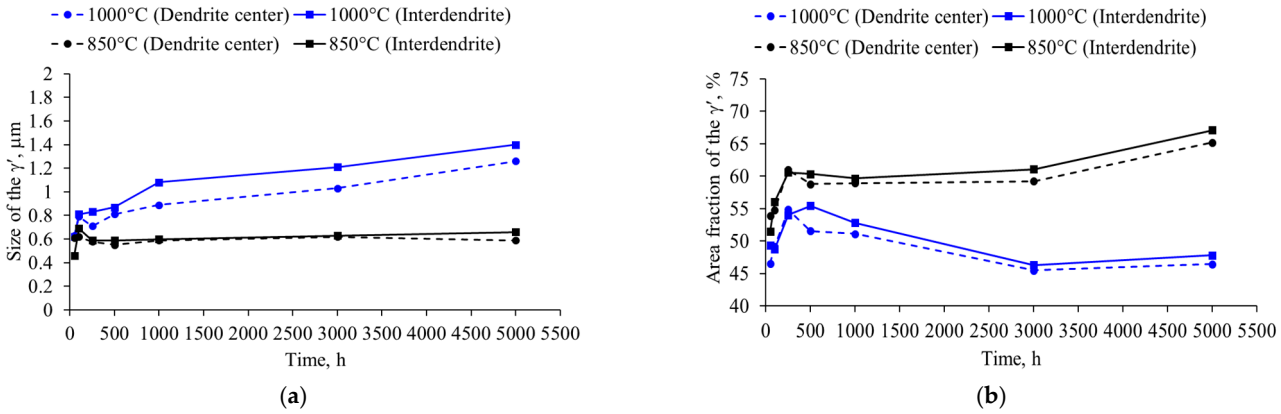


Figure 11. SEM micrographs of the γ′ precipitates of the 850 °C and 1000 °C specimens of different time of durations: (**a**) 850 °C-50 h; (**b**) 850 °C-250 h; (**c**) 850 °C-1000 h; (**d**) 850 °C-5000 h; (**e**) 1000 °C-50 h; (**f**) 1000 °C-250 h; (**g**) 1000 °C-1000 h; (**h**) 1000 °C-5000 h.



(**a**) (**b**)

Figure 12. Quantitative data of γ′ precipitates of the 850 °C and 1000 °C specimens at different locations: (**a**) size and (**b**) area fraction.

In addition, the γ′ precipitates in the dendritic cores are finer than those in the interdendritic regions, consistent with findings by Lavakumar et al. [36]. They also reported that the degree of coarsening increases with heat-treatment temperature and duration. This coarsening is driven by Ostwald ripening: during long-term high-temperature exposure, finer γ′ precipitates dissolve into the matrix, and the solute atoms diffuse to adjacent larger precipitates, promoting their growth [36,37]. Consequently, at high temperatures, the size (or volume fraction) of the smaller secondary γ′ precipitates decreases, while the primary γ′ precipitates significantly increase in size.

3.4. Morphology of the Carbides in the Matrix

3.4.1. MC Carbide

In the specimens heat-treated at 850 °C and 1000 °C, blocky and Chinese script-like MC carbides appear as "white" precipitates (bright contrast) and are concentrated in the interdendritic regions, as shown in Figure 13. This distinct MC carbide morphology is consistent with observations in other Ni-based superalloys [38–40].

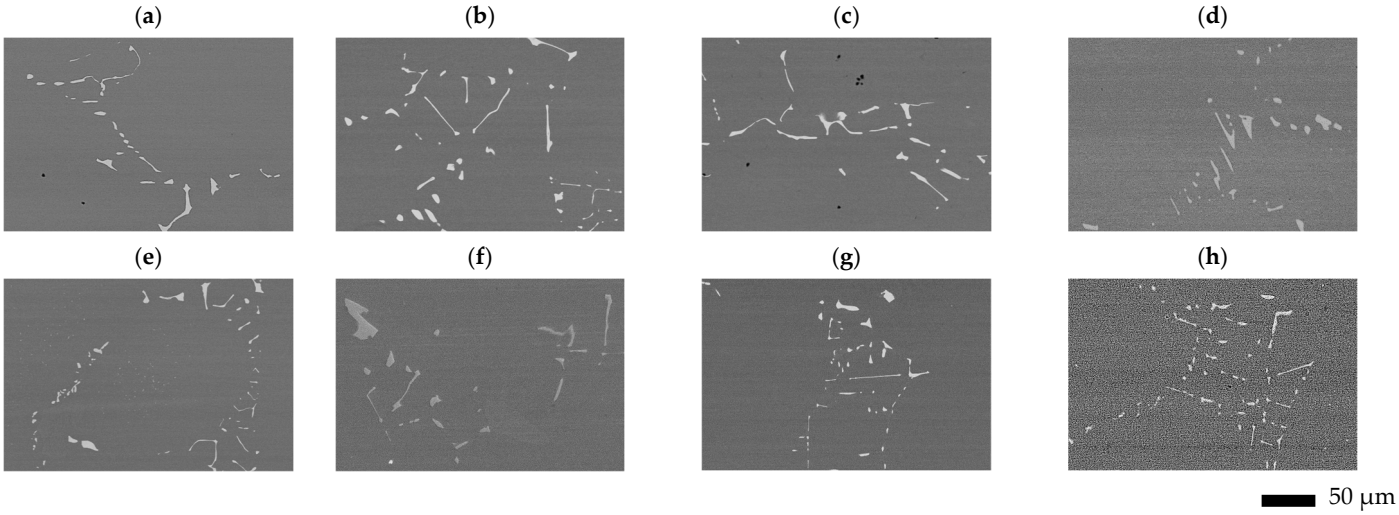


Figure 13. Backscattered SEM micrographs of the carbides of the 850 °C and 1000 °C specimens at different durations: (**a**) 850 °C-50 h; (**b**) 850 °C-250 h; (**c**) 850 °C-1000 h; (**d**) 850 °C-5000 h; (**e**) 1000 °C-50 h; (**f**) 1000 °C-250 h; (**g**) 1000 °C-1000 h; (**h**) 1000 °C-5000 h.

3.4.2. $M_{23}C_6$ Carbide

During high-temperature treatment, MC carbides may transform into $M_{23}C_6$ and/or M_6C carbides, a process accompanied by changes in precipitate size and morphology [41].

$$MC + \gamma \longrightarrow M_{23}C_6 + \gamma' \quad (11)$$

$$MC + \gamma \longrightarrow M_6C + \gamma' \quad (12)$$

Figure 14 illustrates the distribution of carbide phases. The (Ta, Ti, W)C (MC) carbides, depicted in blue, exhibit Chinese script-like and blocky morphologies and are located within the interdendritic regions and at the domain boundaries.

Distinct types of $M_{23}C_6$ carbides were also identified:

Mo-rich $M_{23}C_6$: Appeared as blocky precipitates in the interdendritic regions and at the edges of MC carbides.

W-rich $M_{23}C_6$ $(W,Cr,Mo,Ta)_{23}C_6$: Appeared as rod-like precipitates along the domain boundaries and in the interdendritic regions.

Cr-rich $(Cr,Mo)_{23}C_6$: Exhibited cubic and rod-like shapes, also found at the domain boundaries and in the interdendritic regions.

The distinct spatial distribution of these Mo-, W-, and Cr-rich $M_{23}C_6$ variants is attributed to local chemical heterogeneity. Notably, the formation of Mo-rich $M_{23}C_6$ carbides at the edges of MC carbides is likely driven by localized chemical composition gradients and thermodynamic stability during decomposition [42,43].

The typical composition (in wt.%) is shown in Figure 15. The high concentration of heavy elements, particularly Ta and W, explains why these carbides appear significantly brighter than the surrounding phases in backscattered electron (BSE) SEM micrographs [44].

The volume fraction of blocky MC carbides increased with both temperature and exposure time. Similarly, Dong et al. reported that MC carbides contained high concentrations of Ti and Ta with smaller amounts of W, generally consistent with the stoichiometry (Ti, Ta, W)C [45].

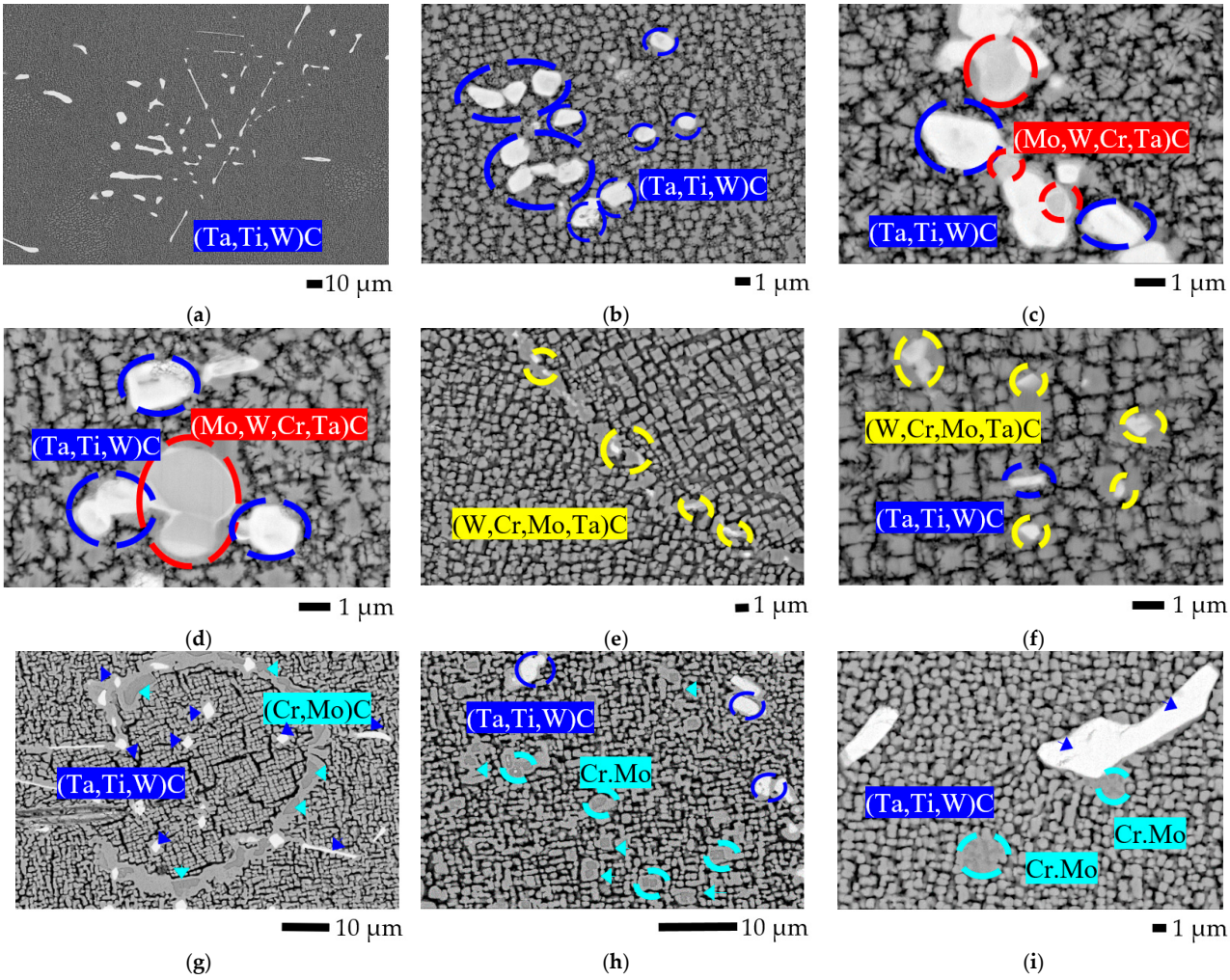


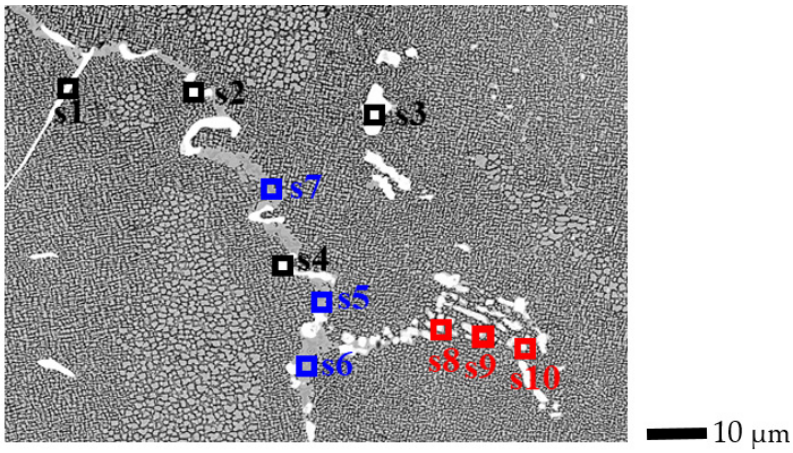
Figure 14. SEM micrographs of the 4 types of carbides of the 850 °C and 1000 °C specimens: (**a**) Chinese script-like and blocky MC carbides; (**b**) Blocky MC carbides; (**c**) Spherical Mo-rich $M_{23}C_6$ and blocky MC carbides; (**d**) Spherical Mo-rich $M_{23}C_6$ and blocky MC carbides; (**e**) Rod-like W-rich $M_{23}C_6$ carbides; (**f**) Rod-like W-rich $M_{23}C_6$ carbides and MC carbides; (**g**) Irregular-shaped Cr-rich $M_{23}C_6$ and MC carbides; (**h**) Cubic-shaped Cr-rich $M_{23}C_6$ and MC carbides; (**i**) Irregular-shaped Cr-rich $M_{23}C_6$ and MC carbides.

3.5. Mechanical Property

Table 4 and Figure 16 present the mechanical properties obtained from the tensile tests. As expected, with increasing temperature, both the yield strength (YS) and ultimate tensile strength (UTS) decrease, whereas the ductility—measured as elongation and reduction in area—increases. As shown in Figure 16, the yield strength and UTS values are highly consistent (showing minimal variation), whereas the elongation and reduction in area exhibit significant scatter, ranging from 20% to 50%.

Table 4. Results of the tensile test.

#	Part of the Specimen	Temperature, °C	YS, MPa	UTS, MPa	Elongation, %	RA, %
1	Airfoil (AF)	25	1150	1295	7.4	10.8
2		800	1031	1201	18.9	25.7
3		900	595	808	15.3	30.2
4	Root (RT)	25	1223	1303	4.5	15.2
5		800	1002	1169	11.7	26.6
6		900	672	831	11.7	33.6



Element	(Ta,Ti,W)C				(Cr,W,Mo)C			(Mo,W,Cr,Ta)C		
	S1	S2	S3	S4	S5	S6	S7	S8	S9	S10
C	13.17	12.92	13.59	12.72	11.05	10.58	10.07	8.43	8.60	8.48
Ti	13.54	14.22	16.13	14.44	0.84	1.08	0.63	2.55	2.38	2.93
Ta	60.85	61.86	58.35	61.24	-	-	0.12	10.93	10.09	12.70
Cr	0.78	0.70	0.68	0.77	57.54	54.63	61.03	17.81	17.45	18.13
Mo	1.57	1.66	1.94	1.66	7.12	6.72	7.44	25.54	25.62	25.28
W	5.03	3.90	5.68	4.64	8.77	9.19	8.81	24.95	26.20	23.91

Figure 15. SEM EDX point analysis for carbides in 850 °C-100 h specimen.

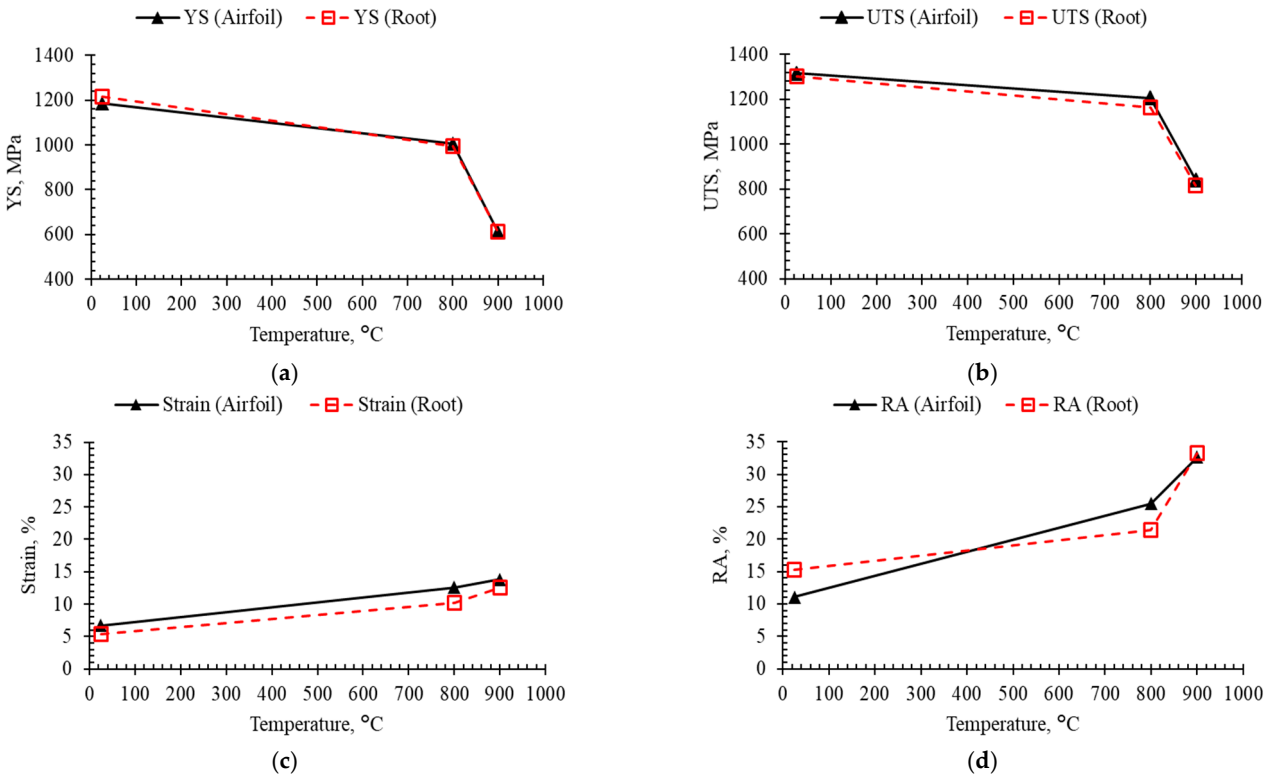


Figure 16. The mechanical properties of the tensile specimens: (**a**) Yield strength, (**b**) Ultimate tensile strength, (**c**) Elongation and (**d**) Reduction in area.

Table 5 summarizes the stress-rupture data for the tested conditions. The results indicate a clear decrease in rupture time as the test temperature increased.

Table 5. Results of the stress-rupture test.

Temperature °C (°F)	Stress, MPa (ksi)	Rupture hr. Airfoil (AF)	Rupture hr. Root (RT)
816 (1500)	428 (62)	1239.3	765.2
871 (1600)	345 (50)	420.1	217.5
926 (1700)	241 (35)	308.3	252.3
982 (1800)	172 (25)	183.5	144.4

3.6. Microstructure of the Tensile Tested Specimen

Figure 17 presents OM micrographs of the tensile specimens etched with K2 solution, clearly revealing a dendritic microstructure and the distribution of carbides. Figure 17 displays microcracks observed along with the rows of the γ' phase. These cracks are likely artifacts introduced during the etching process. The propagation direction of the microcracks is oriented vertically (from top to bottom) to the tensile direction.

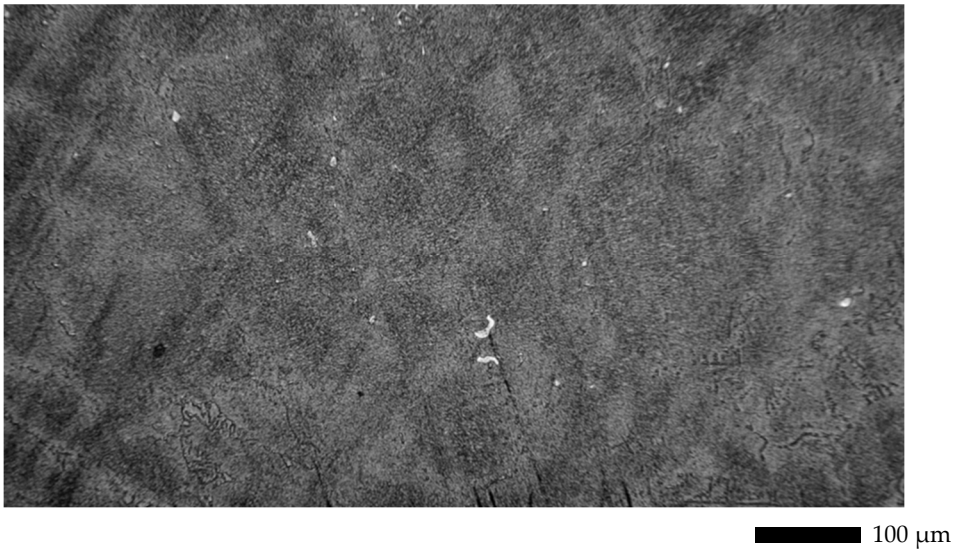


Figure 17. OM micrographs of the dendrite microstructures of the tensile specimen at 900 °C.

Figure 18 demonstrates that cracks were absent in the unetched condition but appeared subsequent to etching. Furthermore, the crack length increased with prolonged etching time. This observation aligns with the findings of Ejaz et al. [46] on the coarsening of the Udimet-500 superalloy, which confirmed that such cracks are merely artifacts induced by the chemical etchant. The fracture surfaces of the tensile-tested specimens were examined using SEM to determine the effect of temperature on the fracture mechanism.

Figure 19 illustrates the fracture surface morphology of the specimens tested at 25 °C, 800 °C, and 900 °C. The fracture surface morphology of the tensile-tested specimens (AF-25 °C/1150 MPa, AF-800 °C/1023 MPa, and AF-900 °C/595 MPa) exhibited a gradual transition. As the test temperature increased, the fracture mode shifted from brittle cleavage to ductile rupture:

1. AF-25 °C (1150 MPa): Exhibited predominantly cleavage (brittle) fracture morphology.
2. AF-800 °C (1023 MPa): Displayed a mixed mode of cleavage and ductile fracture features.
3. AF-900 °C (595 MPa): Showed a fully ductile fracture morphology characterized by dimples.

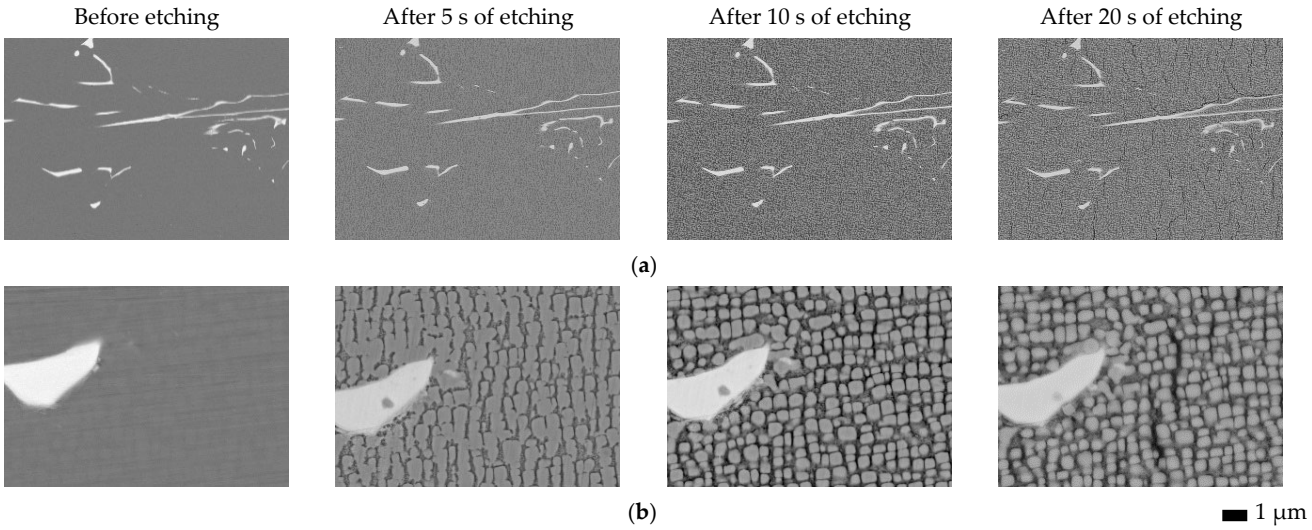


Figure 18. SEM/BSE micrographs of the AF-900 °C-595 MPa tensile specimen: (**a**) at low magnification; (**b**) at high magnification.

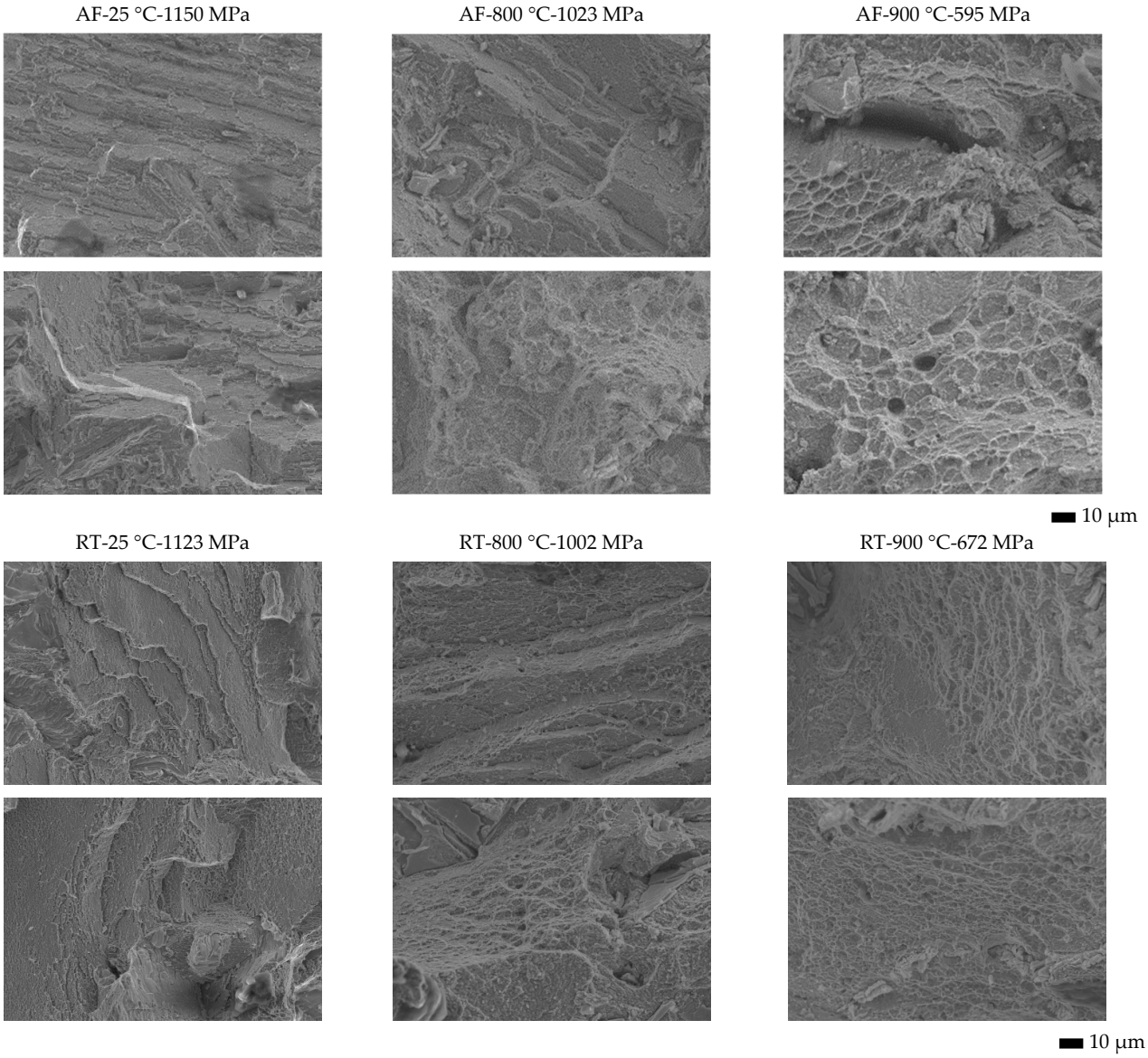


Figure 19. Fracture surface morphology of the tensile specimens.

Specifically, at 800 °C, the prevalence of cleavage steps decreased while dimple formation increased, indicating that the material underwent a brittle-to-ductile transition around this temperature.

Fracture behaviors of the root and airfoil sections were consistent at equivalent temperatures. Similar to the airfoil specimens, the root specimens transitioned from brittle to ductile fracture: predominantly cleavage at 25 °C (RT-25 °C, 1223 MPa), mixed cleavage and ductile features at 800 °C (RT-800 °C, 1002 MPa), and fully ductile dimples at 900 °C (RT-900 °C, 672 MPa).

Figure 20 shows numerous fractured MC carbides (bright precipitates) containing internal cracks. Their high density on the fracture surface suggests they significantly influenced the failure mechanism.

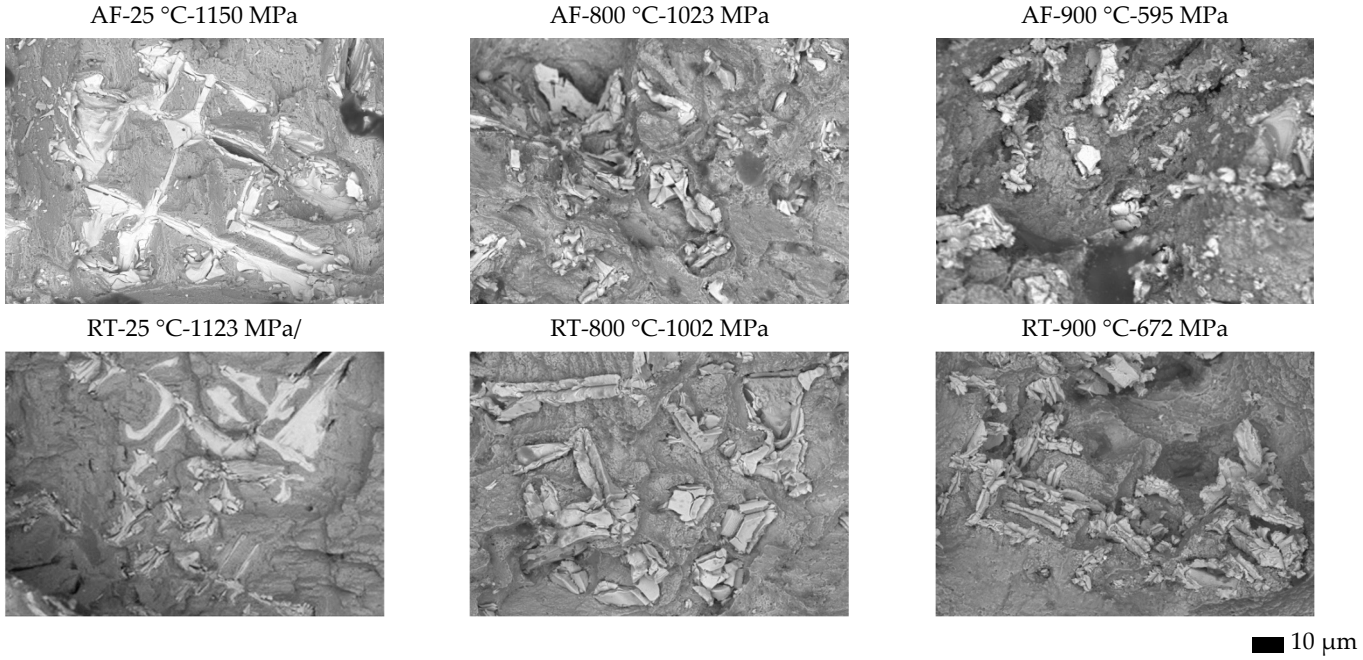


Figure 20. MC carbides on the fracture surfaces of the tensile tested specimens.

Furthermore, EDS analysis confirmed that the abundant bright precipitates are Chinese script-like and blocky MC carbides with a (Ta, Ti, W)C composition (Figure 21). These carbides are known to be thermally stable and contribute significantly to the strengthening of the alloy at elevated temperatures [47]. As shown in Figure 21, cracks were observed within the MC carbides, indicating that these precipitates act as crack initiation sites. Due to the inherent brittleness of the (Ta,Ti,W)C carbides, they crack easily under stress. This premature cracking facilitates crack propagation into the surrounding matrix, thereby significantly reducing the overall fracture toughness of the alloy.

3.7. Microstructure of the Stress-Rupture Specimens

Figure 22 shows that the stress-rupture fracture surfaces were covered with dimples, with diameters between ~6 and ~14 μm. A ductile fracture morphology was dominant in all stress-rupture specimens, with carbides frequently observed on the fracture surfaces. Notably, the average dimple size increased with increasing test temperature.

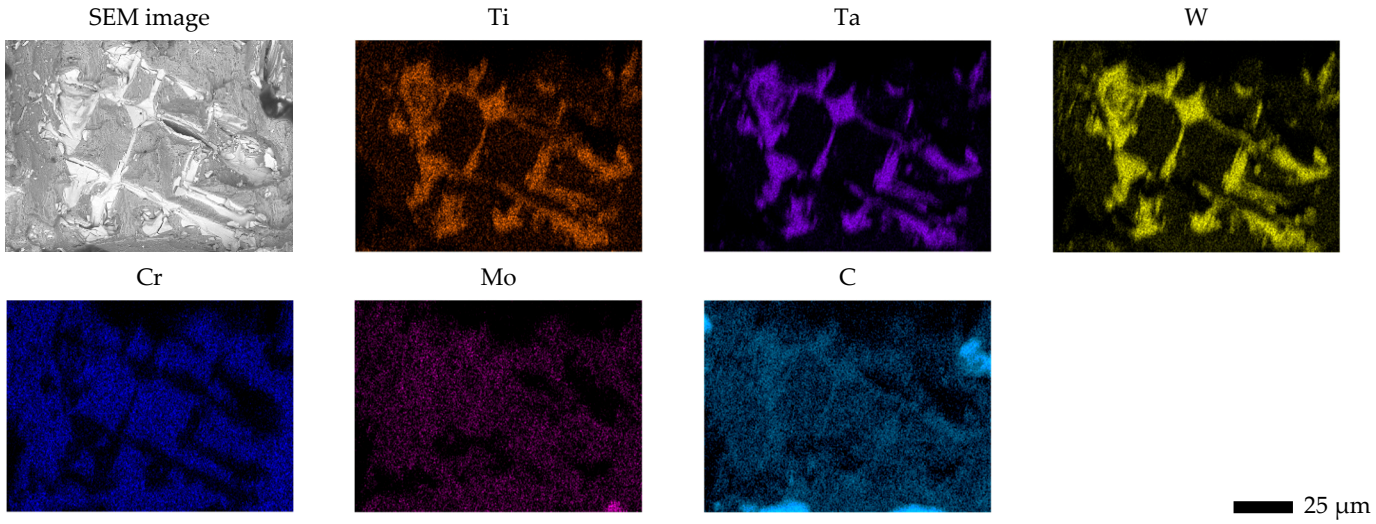


Figure 21. SEM/EDS analyses of the MC carbides on the fracture surface of the tensile specimens.

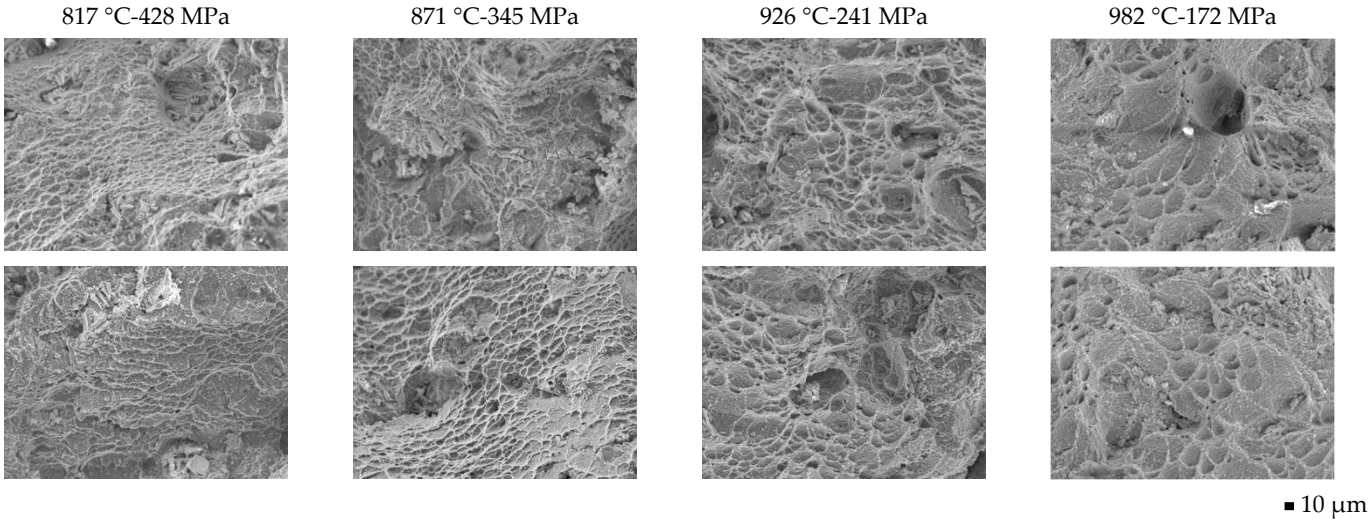


Figure 22. Fracture micrographs of the stress-rupture specimens.

Figure 23 presents the estimated ductile fracture area fractions for the stress-rupture specimens. The results indicate that the area of ductile fracture in the airfoil specimens increased with increasing temperature.

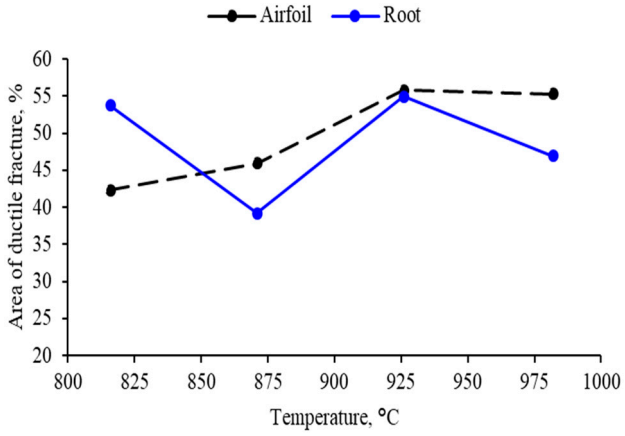


Figure 23. The area of the ductile fracture of the stress rupture specimen.

4. Conclusions

The turbine blade specimens exhibited a dendritic solidification structure composed of dendrite domains. Within the interdendritic regions, Chinese script-like MC carbides and eutectic phases were observed. Crucially, these MC carbides acted as crack initiation sites and provided key propagation paths during both tensile and stress-rupture tests.

1. γ' Precipitates: The morphology of the γ' precipitates evolved with increasing temperature, while their size varied depending on the dendritic location. It is concluded that the γ' precipitates coarsen with increasing heat treatment temperature and duration. This microstructural degradation is associated with the observed deterioration of mechanical properties.
2. Carbides: Four carbide variants were identified in the 850 °C and 1000 °C specimens: MC, and three types of $M_{23}C_6$ (Mo-rich, W-rich, and Cr-rich). MC carbides, characterized by Chinese script-like and blocky morphologies, were observed in the interdendritic regions. Regarding the $M_{23}C_6$ phase: spherical Mo-rich $(Mo,W,Cr,Ta)_{23}C_6$ carbides formed at the edges of MC carbides, irregular Cr-rich $(Cr,W,Mo)_{23}C_6$ carbides precipitated at domain boundaries, and W-rich $(W,Cr,Mo,Ta)_{23}C_6$ carbides appeared as rod-shaped precipitates.
3. Surface Oxidation: The sequential formation of oxide layers—comprising Cr_2O_3, NiO, and TiO_2 at the outermost layer, Ta_2O_5 in the sublayer, and Al_2O_3 at the inner layer—is consistent with thermodynamic predictions and the Ellingham diagram. Morphologically, the Al_2O_3 formed as discontinuous islands in the 850 °C specimens, whereas it coalesced to form continuous oxide layers in the 1000 °C specimens. A Ti-containing phase was observed forming beneath the Al_2O_3 layer, initiating in the 850 °C-1000 h specimen. The oxide layer growth followed the parabolic rate law, increasing with temperature and time. The parabolic rate constants (K) were determined to be 0.0173 $\mu m^2/h$ at 850 °C and 0.2903 $\mu m^2/h$ at 1000 °C. The activation energy for oxidation was calculated as 223.5 kJ/mol, which is comparable to the activation energy for Cr^{3+} diffusion (255 kJ/mol). This suggests that the oxidation process is primarily controlled by the diffusion of Cr^{3+} ions.
4. Tensile Fracture Behavior: The fracture morphologies of the airfoil and root specimens were consistent at equivalent temperatures. A clear brittle-to-ductile transition was observed as the test temperature increased. Mechanistically, the initial cracks formed within the MC carbides, identifying them as the primary crack initiation sites. These cracks propagated through the brittle (Ta,Ti,W)C phase, facilitating the final failure of the specimen.
5. Stress-Rupture Fracture Behavior: A ductile fracture morphology was dominant in all stress-rupture specimens. Notably, the average dimple size on the fracture surfaces increased with increasing test temperature.

Author Contributions: For research articles, the individual contributions are as follows. Conceptualization, J.J., K.S. and J.-H.L.; methodology, Y.K. (Youngdae Kim) and Y.K. (Yeonkwan Kang); software, O.R. and N.-E.B.; validation, Y.H., K.S. and J.-H.L.; formal analysis, O.R. and N.-E.B.; investigation, O.R., N.-E.B. and Y.K. (Youngdae Kim); resources, Y.K. (Youngdae Kim); data curation, O.R. and N.-E.B.; writing—original draft preparation, O.R. and N.-E.B.; writing—review and editing, Y.H., K.S. and J.-H.L.; visualization, O.R. and N.-E.B.; supervision, Y.H., K.S. and J.-H.L.; project administration, Y.K. (Yeonkwan Kang), J.J., K.S. and J.-H.L.; funding acquisition, Y.K. (Yeonkwan Kang), J.J., K.S. and J.-H.L. All authors have read and agreed to the published version of the manuscript.

Funding: This research was supported by the Korea Institute of Energy Technology Evaluation and Planning (KETEP) grant funded by the government of Korea (MOTIE) (20217410100050, Field-Test of Repair Technology on Hot-Gas-Path of Gas Turbine) and KETEP grant funded by the government

of Korea (MOTIE) (RS-2021-KP002514, Development of R&D Engineers for Combined Cycle Power Plant Technologies). The specimens in this study were provided by KEPCO KPS.

Data Availability Statement: The original contributions presented in this study are included in the article. Further inquiries can be directed to the corresponding authors.

Conflicts of Interest: The authors declare no conflicts of interest. The funders had no role in the design of the study; in the collection, analyses, or interpretation of data; in the writing of the manuscript; or in the decision to publish the results.

References

1. Reed, R.C. *The Superalloys: Fundamentals and Applications*; Cambridge University Press: Cambridge, UK, 2006; pp. 128–130.
2. Liu, C.T.; Ma, J.; Sun, X.F. Oxidation behavior of a single-crystal Ni-base superalloy between 900 and 1000 °C in air. *J. Alloys Compd.* **2010**, *491*, 522–526. [CrossRef]
3. Sajjadi, S.A.; Nategh, S.; Guthrie, R.I.L. Study of microstructure and mechanical properties of high performance Ni-base superalloy GTD-111. *Mater. Sci. Eng. A* **2002**, *325*, 484–489. [CrossRef]
4. Ghorbani, H.; Farhangi, H.; Malekan, M. Material Characterization of Long-Term Service-Exposed GTD-111 Nickel Based Superalloy. *Eng. Fail. Anal.* **2023**, *148*, 107061. [CrossRef]
5. Ghorbani, H.; Farhangi, H.; Malekan, M. Microstructural Investigation and Creep Behavior of Long-Term Exposed Directionally Solidified GTD-111 Nickel Based Superalloy. *Mater. Sci. Eng. A* **2024**, *890*, 145811. [CrossRef]
6. Wang, X.; Cui, Y.; Zhou, Y.; Li, Z.; Zhao, Y.; Wang, J. The Microstructure Evolution of a Ni-Based Superalloy Turbine Blade at Elevated Temperature. *Coatings* **2025**, *15*, 835. [CrossRef]
7. León-Henao, H.; Herderick, E.D.; Toro, A.; Giraldo-Barrada, J.E.; Ramirez, A.J. Assessing the Printability of Rene 65 Powder for Repairing Degraded GTD 111 Gas Turbine Blades Using L-DED and L-PBF. *Coatings* **2025**, *15*, 410. [CrossRef]
8. Brenneman, J.; Wei, J.; Sun, Z.; Liu, L.; Zou, G.; Zhou, Y. Oxidation Behavior of GTD111 Ni-Based Superalloy at 900 °C in Air. *Corros. Sci.* **2015**, *100*, 267–274. [CrossRef]
9. Kónya, G.; Szabó, N.; Kovács, Z.F. Investigation of the Machinability of GTD-111 Type Nickel-Base Superalloy During Face Milling. *Acta Mater. Transylvanica* **2023**, *6*, 23–28. [CrossRef]
10. Sajjadi, S.A.; Nategh, S. A high temperature deformation mechanism map for the high performance Ni-base superalloy GTD-111. *Mater. Sci. Eng. A* **2001**, *307*, 158–164. [CrossRef]
11. Hu, Y.-B.; Cheng, C.-Q.; Cao, T.-S.; Zhang, L.; Zhao, J. Film evolution and growth mechanism of a Ni-based superalloy in the two models at different temperatures. *Vacuum* **2021**, *194*, 110538. [CrossRef]
12. Taylor, M.; Ding, R.; Mignanelli, P.; Hardy, M. Oxidation behaviour of a developmental nickel-based alloy and the role of minor elements. *Corros. Sci.* **2022**, *196*, 110002. [CrossRef]
13. Zheng, L.; Zhang, M.C.; Chellali, R.; Bouchikhaoui, H.; Dong, J.X. Oxidation property of powder metallurgy EP741NP Ni-based superalloy at elevated temperatures. *Mater. Technol.* **2013**, *28*, 122–128. [CrossRef]
14. Hou, X.M.; Chou, K.C. Quantitative interpretation of the parabolic and nonparabolic oxidation behavior of nitride ceramic. *J. Eur. Ceram. Soc.* **2009**, *29*, 517–523. [CrossRef]
15. Tan, T.; Chen, Y.; Chen, H. A diffusion controlling duplex-layer oxidation model with scale removal in oxygen containing liquid metal flow. *Comput. Mater. Sci.* **2008**, *44*, 750–759. [CrossRef]
16. Sajjadi, S.A.; Zebarjad, S.M. Study of fracture mechanisms of a Ni-base superalloy at different temperatures. *J. Achiev. Mater. Manuf. Eng.* **2006**, *18*, 227–230.
17. Liang, T.; Wang, L.; Liu, Y.; Song, X. Roles of script MC carbides on the tensile behavior of laser-welded fusion zone in DZ125L/IN718 joints at 650 °C. *J. Mater. Sci.* **2020**, *55*, 13389–13397. [CrossRef]
18. Pour-Ali, S.; Tavangar, R.; Akhtari, F.; Hejazi, S. High-temperature oxidation behavior of GTD-111 Ni-based superalloy with an ultrafine-grained surface at 900 °C. *Corros. Sci.* **2023**, *212*, 110935. [CrossRef]
19. Yun, D.W.; Seo, S.M.; Jeong, H.W.; Yoo, Y.S. The cyclic oxidation behaviour of Ni-based superalloy GTD-111 with sulphur impurities at 1100 °C. *Corros. Sci.* **2015**, *90*, 392–401. [CrossRef]
20. Battulga, N.-E.; He, Y.; Kim, Y.; Kang, Y.; Jung, J.; Shin, K.; Lee, J.-H. High-Temperature Effects on TGO Growth and Al Depletion in TBCs of Ni-Based Superalloy GTD111. *Coatings* **2025**, *15*, 1145. [CrossRef]
21. Biyamin, S.A.; Shaiful Bahari, A.M.; Ng, G.P.; Sanmugham, T.; Ghazali, R.; Ramli, R.; Azmin, A.N. Microstructure Evaluation of Service Aged and Rejuvenated Nickel Super Alloys Using Hot Isostatic Pressing Treatment. *Malays. J. Microsc.* **2022**, *18*, 245–255. Available online: https://www.researchgate.net/publication/360077242_MICROSTRUCTURE_EVALUATION_OF_SERVICE_AGED_AND_REJUVENATED_NICKEL_SUPER_ALLOYS_USING_HOT_ISOSTATIC_PRESSING_TREATMENT (accessed on 18 November 2025).

22. Balsone, S.J. Nickel-Base Superalloy Materials Technology for Advanced IGT Applications. In *Niobium for High Temperature Applications*; Kim, Y.-W., Carneiro, T., Eds.; TMS (The Minerals, Metals & Materials Society): Warrendale, PA, USA, 2004; pp. 3–9. Available online: https://niobium.tech/-/media/niobiumtech/attachments-biblioteca-tecnica/nt_nickel-base-superalloy-materials-technology-for-advanced-igt-applications.pdf (accessed on 18 November 2025).
23. Yu, S.; Zhan, X.; Liu, F.; Guo, Y.; Wang, Q.; Li, Y.; Wang, Z.; Wang, Z.; Tan, L.; Fan, X.; et al. 900 °C oxidation resistance of Ni-base superalloys alloyed with different refractory elements. *J. Alloys Compd.* **2022**, *904*, 164071. [CrossRef]
24. Cao, J.; Zhang, J.; Chen, R.; Ye, Y.; Hua, Y. High temperature oxidation behavior of Ni-based superalloy GH202. *Mater. Charact.* **2016**, *118*, 122–128. [CrossRef]
25. Pérez-González, F.A.; Garza-Montes-de-Oca, N.F.; Colás, R. High temperature oxidation of the Haynes 282® nickel-based superalloy. *Oxid. Met.* **2014**, *82*, 145–161. [CrossRef]
26. Hamidi, S.; Rahimipour, M.R.; Eshraghi, M.J.; Hadavi, S.M.M.; Esfahani, H. Kinetics and microstructural investigation of high temperature oxidation of IN-738LC superalloy. *J. Mater. Eng. Perform.* **2017**, *26*, 563–570. [CrossRef]
27. Giggins, C.S.; Pettit, F.S. Oxidation of Ni-Cr-Al alloys between 1000° and 1200 °C. *J. Electrochem. Soc.* **1971**, *118*, 1782–1790. [CrossRef]
28. Szczotok, A.; Chmiela, B. Effect of heat treatment on chemical segregation in CMSX-4 nickel-base superalloy. *J. Mater. Eng. Perform.* **2014**, *23*, 2739–2747. [CrossRef]
29. Strutt, V.C.I.; Jenkins, B.M.; Woolrich, J.M.; Appleton, M.; Moody, M.P.; Bagot, P.A.J. Effect of microsegregation and heat treatment on localized compositions in single crystal Ni-based superalloys. *J. Alloys Compd.* **2023**, *949*, 169861. [CrossRef]
30. Wang, J.; Xue, H.; Wang, Y. Oxidation behavior of Ni-based superalloy GH738 in static air between 800 and 1000 °C. *Rare Met.* **2021**, *40*, 616–625. [CrossRef]
31. Chen, J.H.; Rogers, P.M.; Little, J.A. Oxidation behavior of several chromia-forming commercial nickel-based superalloys. *Oxid. Met.* **1997**, *47*, 381–410. [CrossRef]
32. Zheng, L.; Zhang, M.; Dong, J. Oxidation behavior and mechanism of powder metallurgy Rene-95 nickel based superalloy between 800 °C and 1000 °C. *Appl. Surf. Sci.* **2010**, *256*, 7510–7515. [CrossRef]
33. Falk-Windisch, H.; Svensson, J.-E.; Froitzheim, J. The Effect of Temperature on Chromium Vaporization and Oxide Scale Growth on Interconnect Steels for Solid Oxide Fuel Cells. *J. Power Sources* **2015**, *287*, 25–35. [CrossRef]
34. Nguyen, L.; Shi, R.; Wang, Y.; De Graef, M. Quantification of rafting of precipitates in Ni-based superalloys. *Acta Mater.* **2016**, *103*, 322–333. [CrossRef]
35. Wang, H.; Long, H.; Liu, Y.; Zhao, Y.; Li, X.; Yang, G.; Yang, X.; Chen, Y.; Mao, S.; Zhang, Z.; et al. The widening of the solution heat treatment window by the addition of Ru in Ni-based single crystal superalloy. *Mater. Charact.* **2023**, *203*, 113057. [CrossRef]
36. Lavakumar, A.; Singh, P.K.; Srivastava, S.; Kori, S.; Kumar, L.A. Gamma prime coarsening behavior of nickel superalloy supercast 247A after prolonged thermal exposures. *IOSR J. Mech. Civ. Eng.* **2013**, *4*, 37–42.
37. Baldan, A. Review: Progress in Ostwald ripening theories and their applications to nickel-base superalloys. *J. Mater. Sci.* **2002**, *37*, 2171–2202. [CrossRef]
38. Chen, Q.Z.; Jones, C.N.; Knowles, D.M. Effect of alloying chemistry on MC carbide morphology in modified RR2072 and RR2086 SX superalloys. *Scr. Mater.* **2002**, *47*, 669–675. [CrossRef]
39. Yu, Z.-H.; Liu, L.; Zhao, X.-B.; Zhang, W.-G.; Zhang, J.; Fu, H.-Z. Effect of solidification rate on MC-type carbide morphology in single crystal Ni-base superalloy AM3. *Trans. Nonferrous Met. Soc. China* **2010**, *20*, 1835–1840. [CrossRef]
40. Szczotok, A.; Rodak, K. Microstructural studies of carbides in MAR-M247 nickel-based superalloy. *IOP Conf. Ser. Mater. Sci. Eng.* **2012**, *35*, 012006. [CrossRef]
41. Zhu, Z.-Y.; Cai, Y.-F.; Gong, Y.-J.; Shen, G.-P.; Tu, Y.-G.; Zhang, G.-F. Isothermal oxidation behavior and mechanism of a nickel-based superalloy at 1000 °C. *Int. J. Miner. Metall. Mater.* **2017**, *24*, 776–783. [CrossRef]
42. Wang, J.; Zhou, L.; Qin, X.; Sheng, L.; Hou, J.; Guo, J. Primary MC decomposition and its effects on the rupture behaviors in hot-corrosion resistant Ni-based superalloy K444. *Mater. Sci. Eng. A* **2012**, *553*, 14–21. [CrossRef]
43. Huang, Y.; Wang, L.; Liu, Y.; Fu, S.-M. Microstructure evolution of a new directionally solidified Ni-based superalloy after long-term aging at 950 °C up to 1 000 h. *Trans. Nonferrous Met. Soc. China* **2011**, *21*, 2199–2204. [CrossRef]
44. Rakoczy, Ł.; Rutkowski, B.; Grudzień-Rakoczy, M.; Cygan, R.; Ratuszek, W.; Zielińska-Lipiec, A. Analysis of γ' precipitates, carbides and nano-borides in heat-treated Ni-based superalloy using SEM, STEM-EDX and HRSTEM. *Materials* **2020**, *13*, 4452. [CrossRef]
45. Dong, X.; Zhang, X.; Du, K.; Zhou, Y.; Jin, T.; Ye, H. Microstructure of carbides at grain boundaries in nickel based superalloys. *J. Mater. Sci. Technol.* **2012**, *28*, 1031–1038. [CrossRef]

46. Ejaz, N.; Mansoor, M.; Salam, I. Effect of high temperature exposure on the microstructure of Udimet-500 super alloy. *J. Mater. Sci.* **2010**, *45*, 4507–4517. [CrossRef]
47. He, L.Z.; Zheng, Q.; Sun, X.F.; Guan, H.R.; Hu, Z.Q.; Tieu, A.K.; Lu, C.; Zhu, H.T. Effect of heat treatment on microstructures and tensile properties of Ni-base superalloy M963. *Mater. Sci. Eng. A* **2005**, *398*, 128–136. [CrossRef]

Disclaimer/Publisher's Note: The statements, opinions and data contained in all publications are solely those of the individual author(s) and contributor(s) and not of MDPI and/or the editor(s). MDPI and/or the editor(s) disclaim responsibility for any injury to people or property resulting from any ideas, methods, instructions or products referred to in the content.